

Aluminum as promising electrode for Mg₂(Si,Sn)-based thermoelectric devices

Julia Camut^a, Ngan Hoang Pham^{a,b}, Dao Y Nhi Truong^a, Gustavo Castillo-Hernandez^{a,c}, Nader Farahi^a, Mohammad Yasser^a, Eckhard Mueller^{a,c} and Johannes de Boor^a

^a contact address: julia.camut@dlr.de; johannes.deboor@dlr.de, Institute of Materials Research, German Aerospace Center (DLR), Germany

^b Ångström Laboratory, Uppsala University, Sweden

^c Institute of Inorganic and Analytical Chemistry, Justus Liebig University of Giessen, Giessen, Germany

* Julia Camut and Ngan Hoang Pham contributed equally

Abstract

The solid solutions of magnesium silicide and magnesium stannide Mg₂(Si,Sn) are high performance thermoelectric (TE) materials with the advantage of being composed of light, cheap and abundant elements. Therefore, they are especially attractive for the conversion of remnant heat into electricity in fields like the automotive sector or the aerospace industry. The optimization of Mg₂(Si,Sn)-based thermoelectric generators requires establishing a suitable electrode to ensure unhindered conduction of the electrical current through the module. We have tested aluminum for such application and developed a technological process for joining. The obtained functionalized TE legs showed electrical contact resistances below 10 µΩcm² for both p- and n-type materials and the values are preserved or even lowered with annealing. The p-type material is found to be stable and in the n-type, there is no indication for a charge carrier compensation due to the electrode, as was previously reported e.g. for Cu and Ag. Comparison with other reported electrodes shows that aluminum is so far the most suitable electrode for a Mg₂(Si,Sn)-based module.

Introduction

As the need for green energy sources is increasing, thermoelectric generators (TEG) are of significant interest in the field of renewable energy due to their ability to convert waste heat into usable electricity. In many industries , such as aerospace and automotive , a large proportion of the energy is wasted as heat, as it cannot be directly reused in a closed loop [1, 2].

A TEG consists of p- and n-type thermoelectric (TE) elements, referred to as legs, which are arranged electrically in series and thermally in parallel using metal-bonded ceramic plates. [3]. Between the TE material and the metal on the ceramic plate (bridge), a metallic layer is

usually inserted, referred to as electrode. Multiple designs and arrays of TEGs exist, optimized for different applications [4].

The performance of a TEG is assessed by its power output P and its conversion efficiency Φ , which directly depends on the TE material properties and the contact resistances between the TE legs and the electrodes, as shown in the following equations [5]:

$$P = \frac{S^2 \sigma}{2} \frac{NA(T_h - T_c)^2}{(l+n)} \quad (1)$$

$$\Phi = \left(\frac{T_h - T_c}{T_h} \right) \left\{ 2 - \frac{1}{2} \left(\frac{T_h - T_c}{T_h} \right) + \frac{4}{zT_h} \left(\frac{l+n}{l} \right) \right\}^{-1} \quad (2)$$

Where, S and σ are the Seebeck coefficient and electrical conductivity of a thermoelement (a n- or p-type leg), z its figure of merit calculated as $z = \frac{S^2 \sigma}{\kappa}$, where κ is the thermal conductivity. N is the number of thermoelement pairs in the module; A is the cross-sectional area of a thermoelement; T_h and T_c are the temperatures at the hot and cold sides, respectively, of the module; l is the length of a thermoelement; $n = 2\sigma\rho_c$, where ρ_c is the electrical specific contact resistance in Ωcm^2 . This equation assumes equal properties for n- and p-type materials; in case of TEG with more than one leg and unequal properties between n- and p-type materials, the average of the electrical and thermal resistivities should be used. The equations are based on the assumption of constant, i.e. temperature independent properties and neglect the effect of the ceramic plates and the thermal contact resistance. They show that material optimization and contact quality improvement are key parameters to increase the TEG performance for a given temperature range. Standard requirements for industrial use of TEG suggest the use of TE materials with a high figure of merit ($zT \geq 1$) and low electrical contact resistance ($\leq 10\%$ of the TE material resistance) [6].

The TE solid solutions $\text{Mg}_2\text{Si}_{1-x}\text{Sn}_x$ ($x \approx 0.7$) have reproducibly high thermoelectric performance with a figure of merit of up to $zT = 1.4$ for n-type and 0.6 for p-type at 450°C [7-12]. This makes the n-type material one of the best in terms of zT in the mid- to high temperature range, with similar performance to other materials in other temperature ranges, such as CoSb_3 ($zT=1.4$ at 500°C [13]) and SiGe ($zT=1$ at 900°C) [3]. The p-type material remains to be improved but lies in the zT range of other known materials used at similar temperatures, such as HMS ($zT=0.8$ at 500°C [14]), ZnSb ($zT=1.2$ at 370°C [15]) and $\text{CeFe}_4\text{Sb}_{12}$ ($zT=0.8$ at 550°C [17]), although the best p-type materials remain PbTe ($zT=1.8$ at 600°C [16]) and TAGS ($zT=1.8$ at 750°C [18]). Silicide-based materials also have the advantages of being lightweight and inexpensive, which makes them especially suitable for applications where weight plays a decisive role, like the automobile and aerospace industries. $\text{Mg}_2(\text{Si},\text{Sn})$ is less costly yet providing the equivalent performance compared with half-Heusler

and Skutterudites alloys, which are more prominently used in waste heat recovery industry [3, 19].

Some silicide-based modules have already been reported [20-26], showing a performance of 0.9 to 4 % of efficiency and a maximal power density between 0.3 and 1 W/cm², often combining n-type Mg₂Si and p-type HMS legs. The development of a fully Mg₂(Si,Sn)-based TEG is still at an early stage. Gao reported a first attempt at building such a TEG [27], showing a maximum power output of 117 mW for T_h = 440 °C and T_c = 110 °C, however the experimental technique used to build the module is tricky and unoptimized. Furthermore, a suitable electrode for the TE material still remains to be found. In order for the performance to be maintained, the contact of the TE material and the electrode must be physically and chemically stable with time: its contact resistance should remain low and the microstructure should not deteriorate during the TEG lifetime. Of the same importance is the preservation of TE material properties during the joining process, which usually limits the temperature and pressure range that can be used [28], while higher temperatures and pressure are usually more favorable to the establishment of a good contact [29]. Those limitations help define some criteria for potential electrode selection: the electrode and TE material should have similar coefficients of thermal expansion (CTE) to ensure mechanical stability across the application temperature range [30] and the electrode should have a melting point such as the maximum joining temperature should be between 50 and 80% of the electrode melting temperature [29, 31]. Obviously, other fundamental requirements are high electrical and thermal conductivity; however since the electrode materials are usually metallic, these criteria are the most easily fulfilled.

Finding a suitable electrode for the Mg₂(Si,Sn) solid solution was attempted in a couple of studies with electrode materials such as Ni, Ag, Cu and constantan (Ni₄₅Cu₅₅) [32, 33]. All show rather low electrical contact resistances but are unsatisfactory due to several issues. Ni was first tested since it was previously identified as good matching electrode for binary Mg₂Si [34-36]. However, a systematic formation of cracks is reported; which is attributed to the mismatch in CTE (13 for Ni; 16.5-18.5·10⁻⁶ K⁻¹ for Mg₂(Si,Sn)), making this material incompatible as an electrode [32]. A similar issue is reported for constantan electrodes (Ni₄₅Cu₅₅) [33]. Ag and Cu are the electrodes showing the lowest contact resistances (about or below 10 μΩcm²), however they both show an altering of the n-type Seebeck coefficient of the TE material after contacting [32, 33]. Ayachi *et al.* recently established that this was due to the formation of Ag defects in the solid solution lattice during the diffusion process, as the formation energy of those defects is lower than the formation energy of the defects responsible for the n-type conduction [37]. A similar behavior is suspected for the Cu electrodes, which

also massively reacts with the TE material, occasionally causing local delamination of the electrode.

In this study, aluminum was selected as candidate for an electrode for the $Mg_2(Si,Sn)$ material, since it is apparently a poor dopant, unlike Ag and Cu [39, 40]. This metal has the advantages of being abundant and low-priced. Its CTE is larger than the TE material's ($26 \cdot 10^{-6} K^{-1}$ for Al [41], $16.5-17.5 \cdot 10^{-6} K^{-1}$ ($x = 0.6$) and $17.5-18.5 \cdot 10^{-6} K^{-1}$ ($x = 0.7$) for the TE material [32, 42]), however aluminum is malleable so it is believed that this behavior will help accommodate the mechanical stresses due to the CTE difference, unlike for Ni which is much harder. Aluminum has a melting point of $660^{\circ}C$, which is low enough to allow for direct bonding to the TE material, while being high enough to guarantee the electrode's stability across the application temperature range ($<500^{\circ}C$). Concerning the possible reactions which could occur at the interface, the phase diagrams of Al with Si and Sn suggest little formation of complicating intermetallic compounds (IMC) that might degrade the overall performance [43, 44]. It is reported that transient liquid phase bonding of Al to Mg using Sn interlayers leads to the formation of the phase Mg_2Sn , which shows that Mg and Sn preferentially react with each other rather than with Al [45]. The association of aluminum and silicides is reported in one study from Tohei *et al.* [26], where Al is used as a solder to join Mg_2Si legs to Ni electrodes. The contact is established and mechanically strong. No secondary phase is reported to form at the interface. No annealing experiment is reported, nor is the evolution of the transport properties after joining. Aluminum has also been used with other silicides, such as $NiSi$ [46] and $CrSi_2$ [47], where it did not show any reaction with Si while successful bonding was obtained.

In this paper, we show that aluminum can be successfully bonded to p-type and n-type $Mg_2(Si,Sn)$, giving low electrical contact resistances with a clean interface, free of detrimental secondary phases. Annealing experiments confirm that the contact on the p-type material is stable, while the transport properties of the n-type material are altered with annealing time, increasing the value of the absolute Seebeck coefficient.

A comparative annealing experiment is made with a non-contacted sample, in which an increase in absolute Seebeck coefficient is also observed. This shows that the main cause for the change in the n-type TE properties is probably magnesium evaporation. It is also found that the electrical contact resistances remain low, or get even lower with annealing. In this manuscript, we show that a step forward is made towards a future TEG, as aluminum is found to be a reliable electrode for $Mg_2(Si,Sn)$ TE materials.

Materials and methods

The solid solutions $Mg_2(Si,Sn)$ pellets were prepared with the following stoichiometry: $Mg_{2.06}Si_{0.3}Sn_{0.665}Bi_{0.035}$ for n-type and either $Mg_{1.98}Li_{0.02}Si_{0.4}Sn_{0.6}$ or $Mg_{1.98}Li_{0.03}Si_{0.3}Sn_{0.7}$ for p-type following the melting route reported in [33, 38, 48]. 3% excess of Mg was introduced in the n-type samples to compensate for the Mg evaporation occurring during the sintering, which lasts double the time needed for p-type samples. The p-type samples presented in this study have different compositions as the one with $x=0.4$ was first selected due to its higher zT ; but meanwhile the studies from Pham *et al.* and Ayachi *et al.* showed that there could be a different behavior between the n-type and the p-type samples after contacting; the work was therefore pursued with the $x=0.3$ composition for both n- and p-type to make the comparison easier. The n-type pellets were sintered at 700°C for 20 min at 66 MPa and the p-type pellets at 650°C for 10 min at 66 MPa under vacuum.

The pellets were then manually grinded to a constant thickness with a precision of $\pm 10 \mu m$. The joining step was made either at 450 °C or 500 °C through indirect heating, for 10 minutes with a pressure of 30 MPa under vacuum, at a 1K/s heating rate. A buffer layer of Al_2O_3 powder was introduced under and on top of the pellet and foils, in order to avoid cracking of the TE pellet due to the pressure while joining. For the p-type samples, the joining at 450°C was made with a composition of $x=0.3$ while the joining at 500 °C was made for $x=0.4$. The aluminum foil (99.5%; chemPUR) was grinded with a 4000 SiC paper before the joining process, in order to remove the native oxide layer on its surface. A combined material compaction and electrode sintering is not feasible for the chosen material combination, because the melting point of aluminum is too low compared to the temperature necessary to the good compaction and optimization of the properties of the TE material [49, 50]. The joining temperatures of 450 °C and 500°C were selected as they respect the criteria of being between 50 and 80% of the melting point of aluminum while preserving the TE material properties, which can be altered with an excessively high temperature exposure [49].

The quality of the joining is estimated by the value of its specific contact resistance r_c and the preservation of the Seebeck coefficient of the TE material using a Potential & Seebeck Scanning Microprobe (PSM) [51]; and by its microstructural and chemical composition at the interface using scanning electron microscopy (Zeiss Ultra 55 SEM equipped with an EDX detector). After characterization, the contacted samples are annealed at 450 °C under argon atmosphere for 1 and 2 weeks (total time) with BN coating in order to investigate the contacts stability over time.

An experimental flowchart summing up the sintering, contacting, annealing and analysis of the samples is shown in Figure 1.

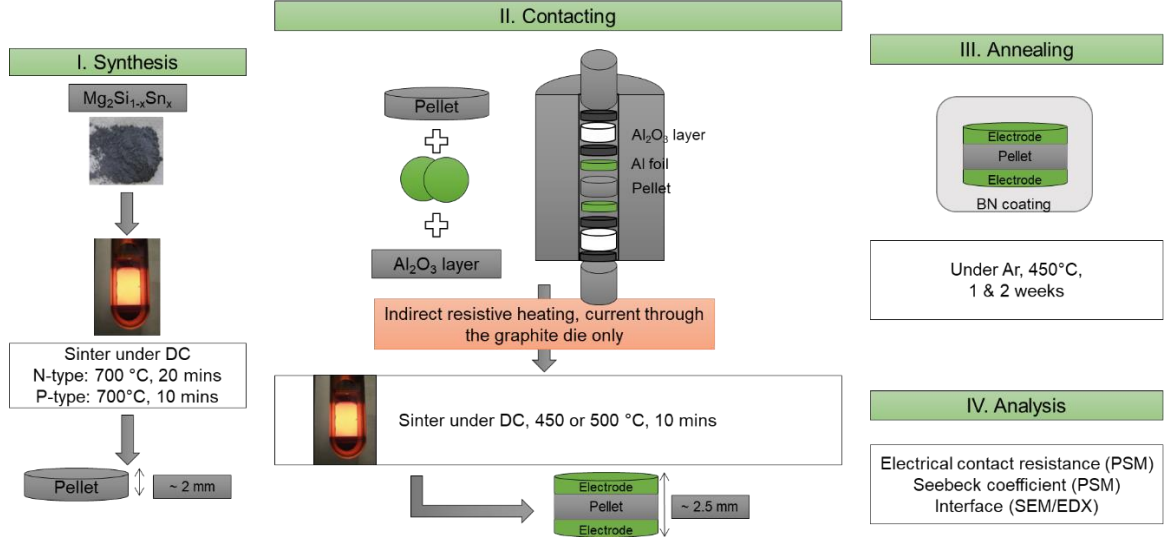


Figure 1 - Experimental flowchart from powder to the analysis of the contacted pellet. After measuring the Seebeck coefficient, it is possible to estimate the carrier concentration and the carrier mobility after annealing using a single parabolic band model (SPB) [52]. In this model, the transport properties are obtained following the equations given by:

$$|S| = \frac{k_B}{e} * \left(\frac{2F_1(\eta)}{F_0(\eta)} - \eta \right) \quad (3)$$

$$n = 4\pi \left(\frac{2m_d^* k_B T}{h^2} \right)^{1,5} F_{\frac{1}{2}}(\eta) \quad (4)$$

Where $\eta = \frac{E_F}{k_B T}$ is the reduced chemical potential, m_d^* the density of states effective mass and n the carrier concentration, k_B is the Boltzmann's constant, $F_i(\eta)$ is the Fermi integral of order i .

Using the Pisarenko plot linking S and n with an effective mass of $2.5 m_0$ for n-type [53] and $1.5 m_0$ for p-type [52], we deduce the carrier concentration of the samples from our measured S data. The plots are shown in Supplementary Information. The electrical conductivity σ is measured with an in-house built system, which allows to measure the electrical conductivity of a sample using a four-point-probe in in-line setup [54], with 1 mm probe distance. The probes are spring-loaded tungsten carbide needles. The voltage measurement for the voltage drop across the sample and the voltage drop across a 1-Ohm reference resistance are done by lock-in-amplifiers for accuracy. The voltage at the reference resistance is needed to calculate the electrical current and thus the sample's resistance, from which the specific resistance or conductivity is calculated; the sample's geometry is taken into account by a calculated correction factor. This device has the advantage of allowing to measure samples with smaller geometries, although if the geometry is too close or smaller than the length of the 4-points distance the results are less accurate. The mobility μ is then calculated using the

electrical conductivity and the Seebeck coefficient estimated carrier concentration, using the following equation:

$$\sigma = ne\mu \quad (5)$$

Results

In general, joining the TE material with Al provides visibly good joints, as can be seen in Figure 2. Sound contact is produced without any visible cracks or delamination either in the material or the electrode foil. The visible black dots in the TE material are a Si-rich phase due to incomplete reaction; those impurities are often seen in the material [49]. The evolution of the microstructure at the interface with joining temperature and annealing is reported in Figure 3. It is seen for all the samples that the interface directly after joining is very flat and smooth and there is no visible indication for a chemical reaction between the aluminum electrode and the TE material. After 1 week of annealing a few black spots at or close to the interface and a brighter layer close to the interface are visible. From EDX line scans (Figure 4) these can be identified as aluminum grains and a Sn-rich $Mg_2(Si,Sn)$ phase at the interface. There is no drastic evolution between the first and the second week of annealing, as the secondary phases do not noticeably grow further. Note that a different piece (cut from a pellet sintered under identical conditions) was employed for each annealing experiment in order to preserve samples at different annealing stages.

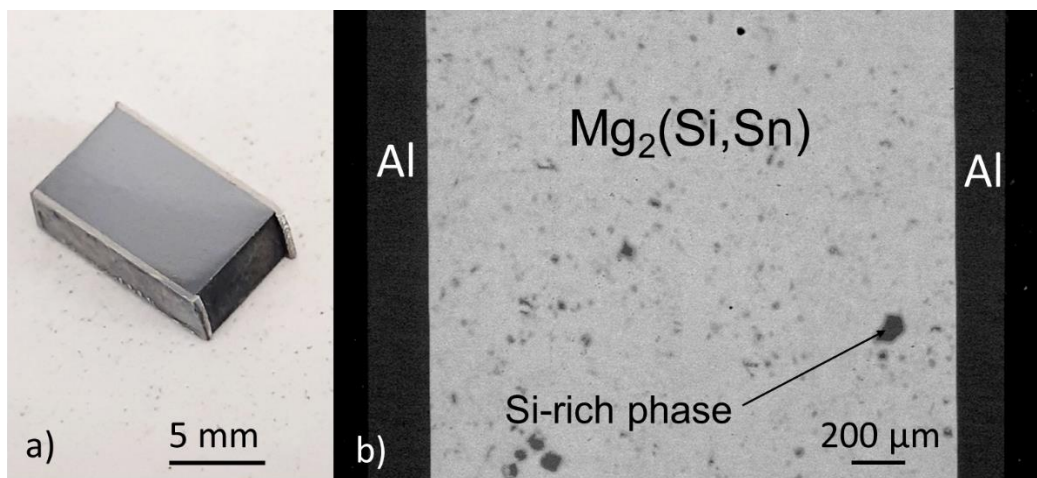


Figure 2 – a) Photo and b) SEM image of a sample after joining

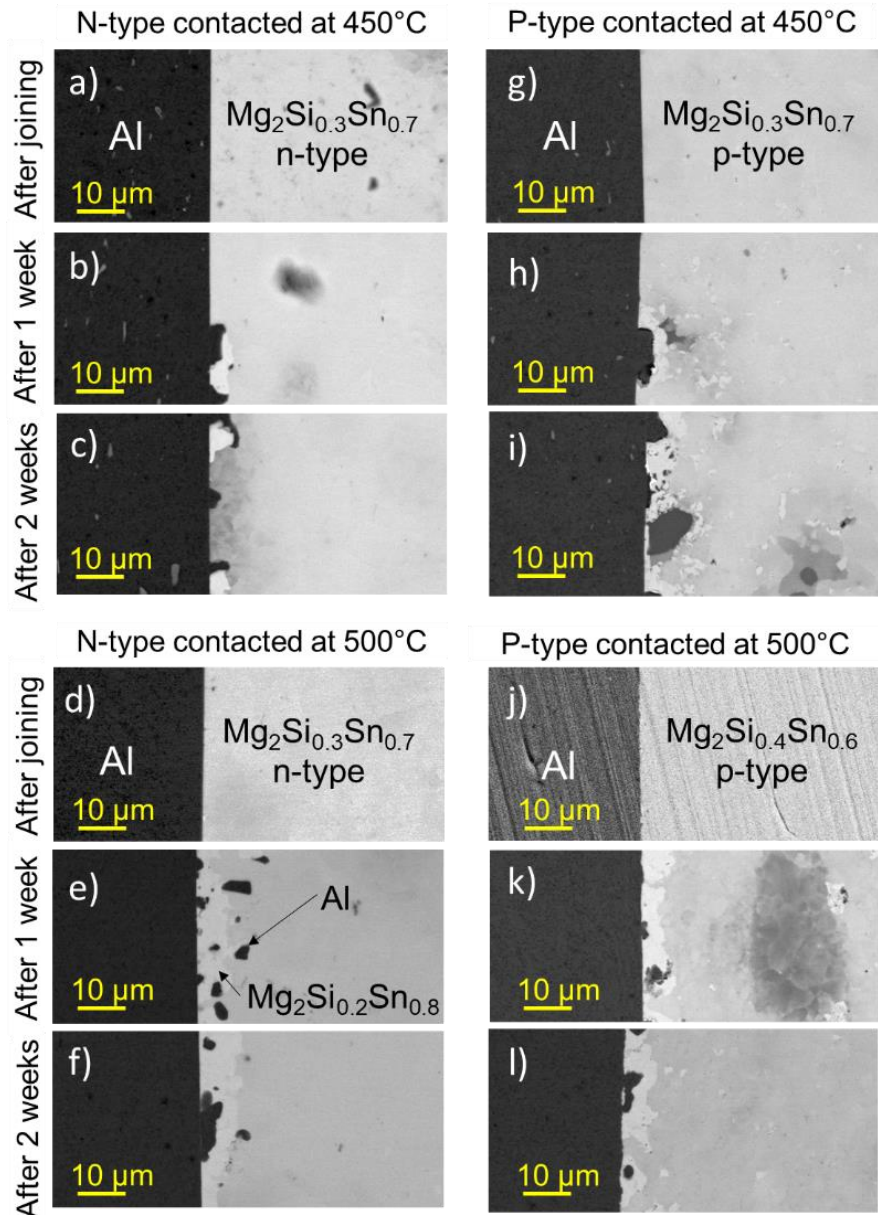


Figure 3 - SEM images of the contacted samples for difference joining temperatures: directly after joining, after 1 and 2 weeks of annealing at 450°C under Ar atmosphere.

From the EDX line scan in Figure 4 the atomic % can be read, corresponding to a composition of approximately $\text{Mg}_2\text{Si}_{0.15}\text{Sn}_{0.85}$ for that newly formed phase. This phase extends on a scale from 5 to 15 μm . The size of this secondary phase differs between the samples. The two samples contacted at 450°C show scarce nuclei along the interface (diameter \approx 5-10 μm), while the samples contacted at 500°C show more or less continuous reaction layers (thickness \approx 10-15 μm). This difference could be due to the difference in joining temperature, although there is no noticeable difference directly after joining. It is possible that Al has diffused more into the TE material with a higher joining temperature, allowing the reaction during annealing to progress faster. This could also simply be due to sample-to-sample variation. The

small Al “particles” found close to the interface might be due to diffusion and precipitation during the cooling process, but the exact mechanism remains unclear.

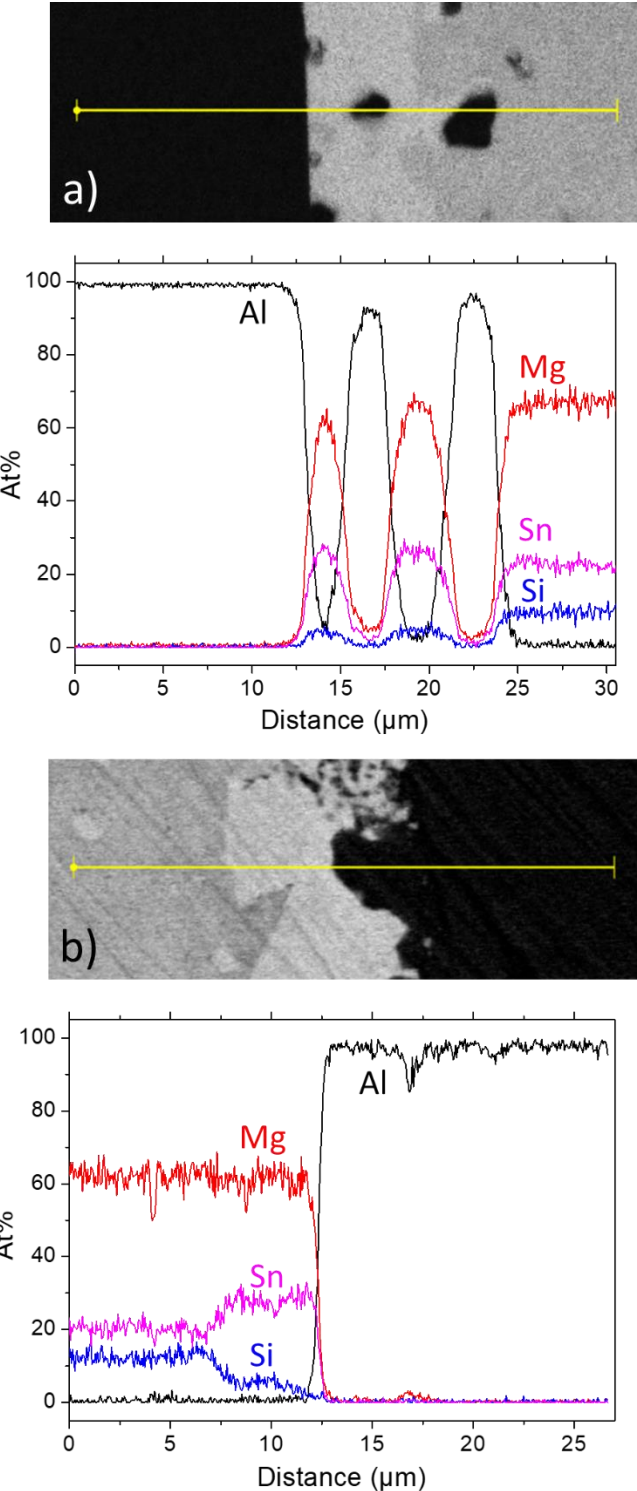


Figure 4 - EDX line-scan of the secondary phases forming at the interface. The samples are a) n-type $Mg_2Si_{0.3}Sn_{0.7}$ and b) p-type $Mg_2Si_{0.4}Sn_{0.6}$ both contacted at 500°C

Figure 5 and Figure 6 show the Seebeck coefficient and potential line-scan for all the samples, p-type and n-type respectively. It can be observed that the absolute potential values

differ quite dramatically for the different samples. This is due to the quality of the interface between the sample and the sample holder, which has a direct impact on the magnitude of the flowing current, roughly proportional to the potential values. This however does not influence the r_c measurement results.

It is seen that the p-type Seebeck coefficient is not changing with annealing, although the measurement of the sample contacted at 450°C and annealed for 1 week shows large scattering. This can be attributed to some problem during the measurement (poorer contact to the sample holder, surface quality or wear of the tip). This explanation is also supported by the fact that no other p-type sample shows this much scattering, which leads to believe that this is rather due to a punctual preparation issue than to the aluminum joining. Overall, the average p-type Seebeck coefficient lies around 90 $\mu\text{V/K}$, corresponding to a carrier concentration of about $1.9 \times 10^{20} \text{ cm}^{-3}$, which is in the usual range reported in literature for optimal properties [7]. However, it is seen that the n-type Seebeck coefficient is altered through annealing. The sample contacted at 450°C shows a Seebeck coefficient evolution from -100 to -130 and -145 $\mu\text{V/K}$ after respectively 1 and 2 weeks of annealing. The sample contacted at 500°C changes from -120 to -180 and -170 $\mu\text{V/K}$ after respectively 1 and 2 weeks of annealing. The change between the first and second week of annealing in both samples can be explained by the PSM accuracy of about 10-15 % [55].

It should be noted that the power factors and figure of merit for the n- and p-type samples at room temperature before annealing are in the range of previously reported high performance samples [48, 52]. The n-type sample shows power factors of about $25 \cdot 10^{-4} \text{ W/mK}^2$ at room temperature and $38 \cdot 10^{-4} \text{ W/mK}^2$ at 700K and a figure of merit $zT=1.3$ at 650 K, while the p-type sample shows power factors of about $6 \cdot 10^{-4} \text{ W/mK}^2$ at room temperature and $12 \cdot 10^{-4} \text{ W/mK}^2$ at 700K and a figure of merit $zT=0.4$ at 650 K. This confirms the good TE properties of the employed material with tested electrodes for future devices.

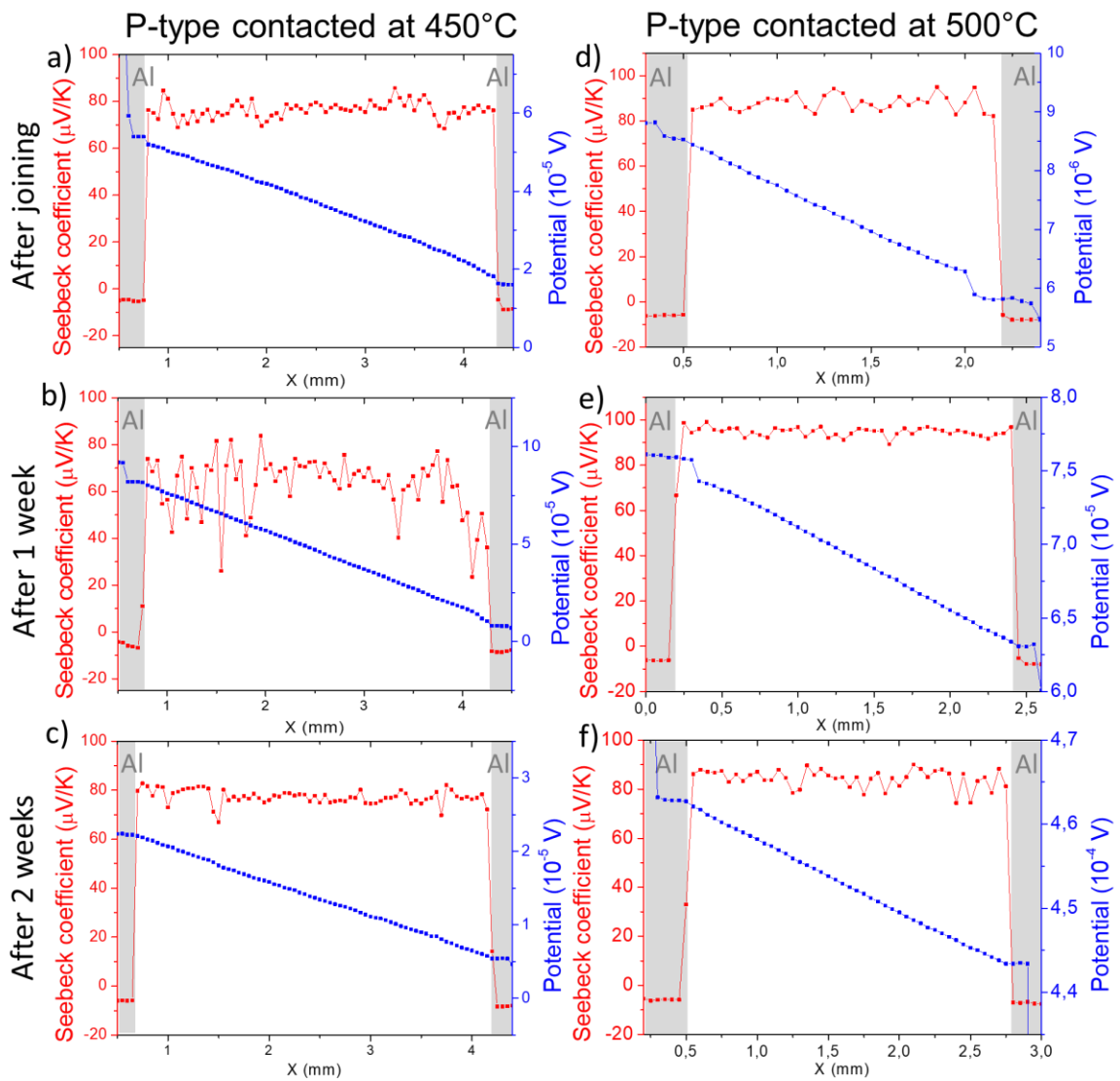


Figure 5 - Exemplary line-scans of the Seebeck coefficient and the electrical potential for p-type $\text{Mg}_2(\text{Si},\text{Sn})$ samples for different joining temperatures: directly after joining, after 1, and after 2 weeks of annealing at 450°C under Ar atmosphere.

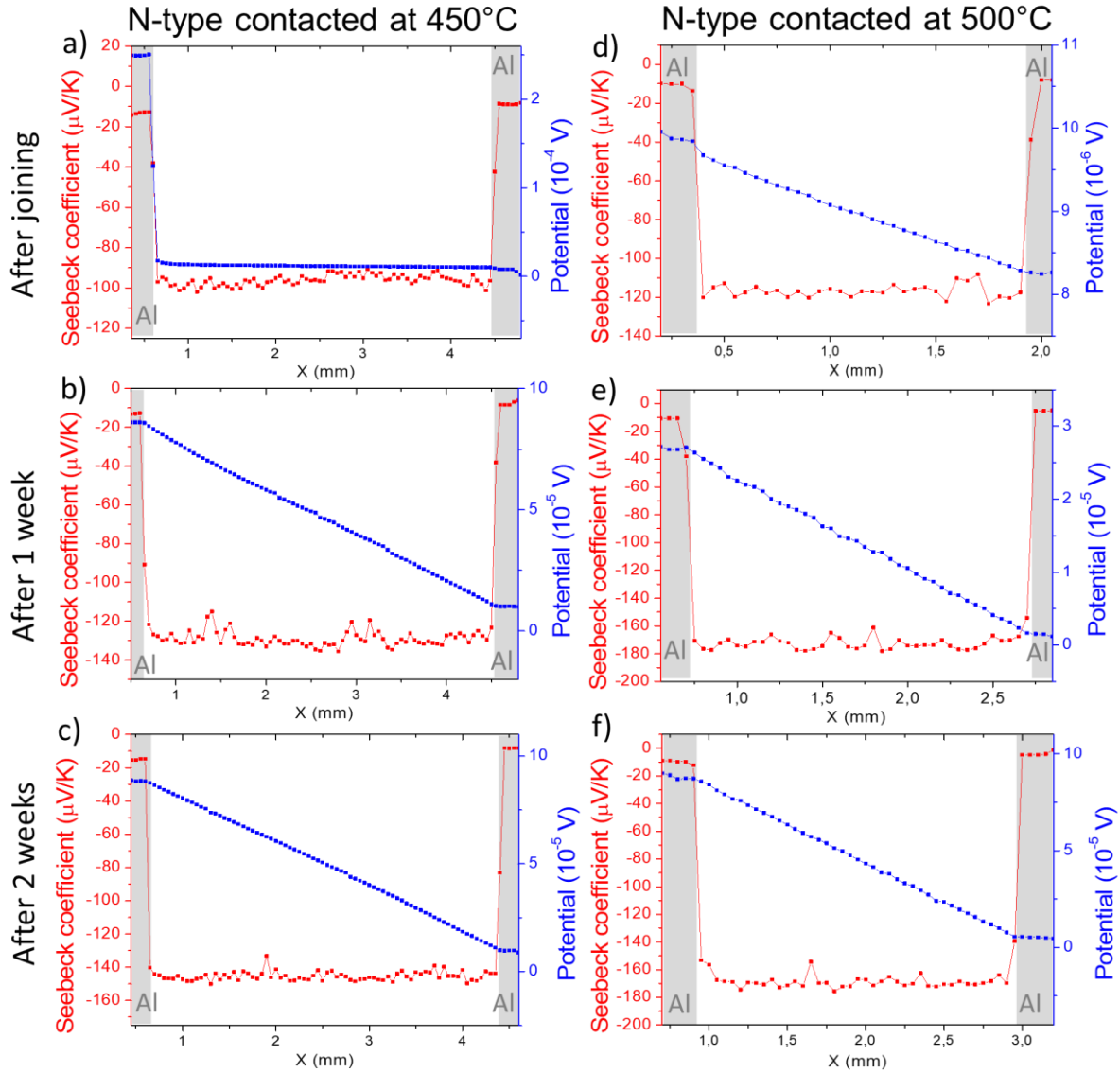


Figure 6 - Exemplary line-scans of the Seebeck coefficient and the electrical potential for the n-type $Mg_2(Si,Sn)$ samples for different joining temperatures: directly after joining, after 1, and after 2 weeks of annealing at $450^\circ C$ under Ar atmosphere.

The specific electrical contact resistance r_c is calculated as previously reported [33], using the following equation:

$$r_c = \frac{(V_{elec} - V_{TE}) * l_{TE}}{\Delta V_{TE} * \sigma_{TE}} \quad (6)$$

Where V_{elec} is the potential on the electrode at the interface and V_{TE} is the potential on the TE material at the interface, the position of interface being located using the drop in Seebeck coefficient on the line-scan. l_{TE} is the length of the TE material (between the two electrodes), ΔV_{TE} is the drop in potential across the TE material and σ_{TE} is the electrical conductivity of the TE material, measured using a 4-probe inline technique. For the samples which were too small

to be measured, a constant charge carrier mobility compared to a similar sample is assumed, and the σ_{TE} is obtained using Eq. 5 by estimating the charge carrier concentration using the Pisarenko plot and the measured Seebeck coefficient. The variation in carrier concentration is then proportional to the variation in electrical conductivity.

The obtained r_c values are compared to contact resistance values obtained using the current density directly measured by the PSM, contrarily to Eq. 6 where the current density is calculated using the TE material properties:

$$r_{c_PSM} = \frac{(V_{elec} - V_{TE}) * A}{I_{PSM}} \quad (7)$$

Where A is the sample cross-section and / the current measured in the device. Multiple line-scans are measured for each sample, the r_c value presented below is the average value of all the lines, given with the corresponding standard deviation.

The calculation of the electrical contact resistance according to Eq. 7 requires the assumption that the current density is homogeneous over the whole sample (along cross-section and length), while Eq. 6 only assumes a constant current density along the direction of the line-scan. The more inhomogeneous the interface, the more different are the results given by both equations.

The r_c value of each sample is reported in Table 1. All samples show a low contact resistance directly after contacting except the n-type sample contacted at 450°C. This sample shows asymmetric r_c contact resistance, the “left/right” designate the left and right interfaces on the PSM scan shown in Figure 6. One of the r_c value is satisfactorily low but the other one is dramatically high ($>1000 \mu\Omega\text{cm}^2$). Moreover, there is a large difference between the results from Eq. 6 and Eq. 7, meaning that the interface of the sample is highly inhomogeneous. The very same piece of sample is used for the first week of annealing and it is seen that annealing seems to “heal” the high contact resistance, as after 1 week of annealing the sample shows symmetric and low r_c and r_{c_PSM} values. Similarly, for the p-type sample contacted at 450°C, the initial r_c value after joining is $17 \pm 8 \mu\Omega\text{cm}^2$, and is progressively decreased with annealing, until reaching a value below $10 \mu\Omega\text{cm}^2$ after 2 weeks. Both samples contacted at 500°C had an initial value $<10 \mu\Omega\text{cm}^2$ directly after joining, which is not altered with annealing. Overall, most r_c values are around or below $10 \mu\Omega\text{cm}^2$, while most r_{c_PSM} values remain below $20 \mu\Omega\text{cm}^2$, which shows acceptable homogeneity and reliability of the measurement.

Table 1 - Specific electrical contact resistances of the Mg₂(Si,Sn) samples for difference joining temperatures: directly after joining, after 1, and after 2 weeks of annealing at 450°C under Ar atmosphere. r_c values were calculated using Eq. 6, r_{c_PSM} using Eq. 7

		Contacted at 450°C		Contacted at 500°C	
p-type	r _c ($\mu\Omega\text{cm}^2$)	r _{c_PSM} ($\mu\Omega\text{cm}^2$)	r _c ($\mu\Omega\text{cm}^2$)	r _{c_PSM} ($\mu\Omega\text{cm}^2$)	
After joining	17 ± 8	19 ± 6	9 ± 5	3 ± 2	
1 week annealing	11 ± 7	13 ± 9	4 ± 2	4 ± 2	
2 weeks annealing	7 ± 3	5 ± 3	9 ± 9	18 ± 18	
n-type	r _c ($\mu\Omega\text{cm}^2$)	r _{c_PSM} ($\mu\Omega\text{cm}^2$)	r _c ($\mu\Omega\text{cm}^2$)	r _{c_PSM} ($\mu\Omega\text{cm}^2$)	
After joining (left/right side)	1327 ± 195 / 10 ± 4	9487 ± 1396 / 69 ± 28	3 ± 2	1 ± 1	
1 week annealing	5 ± 2	8 ± 4	5 ± 6	14 ± 16	
2 weeks annealing	6 ± 3	15 ± 9	5 ± 3	11 ± 8	

The change in Seebeck coefficient of the n-type sample could originate from two factors: the diffusion of Al creating stable defects and changing the carrier concentration in the TE material or the evaporation of Mg due to annealing, previously reported in literature [56]. In order to understand the origin of the change in the n-type Seebeck coefficient with annealing, the results of comparative annealing experiments are reported in Figure 7. Several samples are compared: an electrode-free control sample and the samples contacted at 450°C and 500°C already presented above. All samples are coated with a BN slurry and annealed for 1 and 2 weeks at 450°C under Ar.

The control sample is a pellet which was previously contacted with Al at 450°C and showed very high contact resistance on both sides, indicating that the Al diffusion length into the TE material is very probably negligible. The Al was peeled off and the faces of the TE pellet were thoroughly grinded (>0.1 mm). As a consequence, the sample has a similar thermal history than the other samples while being Al-free.

It is seen that in the control experiment, the Seebeck coefficient gradually changes with annealing, increasing from -90 $\mu\text{V/K}$ to -110 $\mu\text{V/K}$ and -120 $\mu\text{V/K}$ after respectively 1 and 2 weeks of annealing, which demonstrates the effect of Mg loss alone. With similar coating conditions, the sample contacted at 450°C shows a Seebeck coefficient evolution from -100 $\mu\text{V/K}$ to -130 $\mu\text{V/K}$ and -145 $\mu\text{V/K}$: the change after each annealing step is larger than for the control experiment, presumably indicating that some of this evolution is due to the aluminum

electrode. However, those changes remain within the range of error of the PSM and must therefore be considered cautiously. For the experiment with the contacting at 500°C, the Seebeck coefficient goes from -120 µV/K to -180 µV/K after one week and to -170 µV/K after 2 weeks. The decrease in |S| after the first week is within the measurement accuracy of the PSM and most likely not a physical change; we assume that the Seebeck coefficient is reaching a plateau after the first week of annealing.

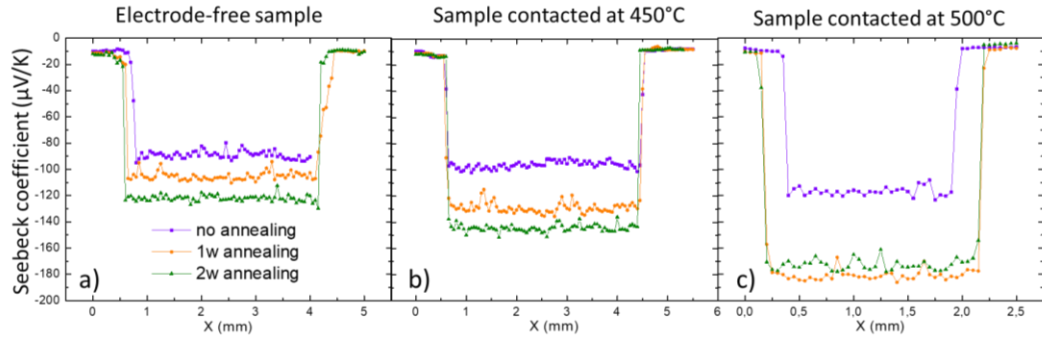


Figure 7 - Evolution of the n-type Seebeck coefficient with annealing for a) the control experiment (sample without electrode), b) the sample contacted at 450°C, c) the sample contacted at 500°C

Using the set of equations 3-5, the mobility of the charge carriers in the control experiment and the sample contacted at 450°C with different annealing times is calculated and reported in Table 2. For both samples, annealing implies a drastic decrease of the electrical conductivity, generally by a factor of 3-4. It can be seen that for the sample contacted at 450°C, the mobility after the first week of annealing is reduced by a factor of 2, and does not change much further after the second week of annealing. The mobility of the control experiment after two weeks of annealing is also reduced by a factor of 2. The sample contacted at 500°C and the corresponding annealed samples were too small to be reliably measured, their charge carrier mobility was therefore not assessed. For the same reason, the electrical conductivity after the first week of annealing for the control experiment could also not be measured.

Table 2 – Measured and estimated electrical properties of the n-type TE material after joining and after 1 and 2 weeks of annealing

Control experiment	0 week	1 week	2 weeks
Av. Seebeck coefficient (µV/K)	-90	-105	-120
Carrier concentration (10^{20} cm^{-3})	4.1	3.2	2.5
Electrical conductivity (S/cm)	3130	-	1190
Mobility (cm ² /Vs)	48	-	30
Contacted at 450°C	0 week	1 week	2 weeks

Av. Seebeck coefficient ($\mu\text{V/K}$)	-95	-130	-145
$n (10^{20} \text{ cm}^{-3})$	3.8	2.1	1.7
Electrical conductivity (S/cm)	3450	1150	840
Mobility (cm^2/Vs)	57	34	31

Discussion

Firstly, there is no sign for a harmful CTE mismatch impact on the pellet as no formation of cracks is observed after joining the electrode. The formation of the Sn-rich phase at the interface with annealing is also interesting in this regard, as Mg_2Sn has a CTE of $17\text{-}19\cdot10^{-6} \text{ K}^{-1}$ [57, 58], so it could act as a mechanical buffer layer between the electrode and $\text{Mg}_2(\text{Si},\text{Sn})$ and enhance the mechanical stability of the joint. Moreover, the microstructure evolves slowly after the first week of annealing, as not much further growth is noticed after the second week, therefore the interface seems also chemically sufficiently stable.

The decrease in r_c with annealing is systematic, even for samples starting with higher values, while the development of the microstructure is not uniform in all the samples. No trend can be observed between the r_c value, its standard deviation and the regularity of the microstructure, meaning that the growth of the reaction layer is not correlated with the electrical contact resistance. Possible explanations for the decrease of r_c with annealing are the reconsolidation of nano-cracks [59, 60] or a dissolution of oxides at the interface which would allow a better current transmission.

The influence of the joining temperature on the quality of the contact is not large in the investigated range. It seems that a higher joining temperature induces a thicker reaction layer at the interface with annealing, which could potentially guarantee a higher mechanical stability. The n-type pellet contacted at 450°C is the only one showing a tremendously high electrical contact resistance (on one side only), but it is believed to be rather due to a punctual lack of process control than to the joining temperature itself, as this is not observed for the p-type equivalent experiment. Nevertheless, contacting at 500°C instead of 450°C provided lower r_c values directly after joining and is therefore found to be advantageous.

The aluminum electrode does not have any detrimental impact on the p-type Seebeck coefficient, even after 2 weeks of annealing. A significant increase is however observed in the n-type absolute Seebeck coefficient, indicating that the carrier concentration decreases with annealing. At least two factors can plausibly be at play in this change: Al diffusing into the TE material and altering its transport properties through the formation of stable compensating defects and Mg evaporation during annealing.

Liu *et al.* showed that in n-type Mg_2Sn and Mg_2Si , the most stable defects are Mg vacancies (-2), independently of Mg chemical potential [61]. If there is some Mg evaporation during annealing, this means that the amount of Mg vacancies increases. This should decrease the electron carrier concentration and thus increase $|S|$. A decrease in carrier concentration under Mg loss has already been observed experimentally for n-type material [49, 56], which supports this hypothesis. One could wonder why such a behavior is not observed on the p-type samples. In this regard it is interesting to note that the n-type material is synthesized containing excess Mg, while the p-type is not [48]. This means that during annealing, the n-type can shift from Mg-rich to Mg-poor condition, while the p-type material remains under Mg-poor conditions all along the annealing experiments. This could explain the fact that the n-type Seebeck coefficient is changing while the p-type is not.

In Figure 7, the control experiment, without the Al electrode, shows an ongoing increase of $|S|$ with annealing duration, well in line with the hypothesis that Mg loss is mainly responsible for the observed changes. For the sample contacted at 450°C the change of $|S|$ after one week is higher than for the control experiment, possibly indicating that an Al-TE interaction also plays a role in the decrease of carrier concentration. The further evolution is comparable to that of the control sample and therefore most likely an indication of ongoing Mg loss. The sample contacted at 500°C shows a significantly larger change than the other two. This could again be due to Mg loss, with the higher change being linked to the higher joining temperature, and/or and to the interaction of the Al electrode with the TE material.

A generally possible interaction mechanism (diffusion of the electrode into the TE material) was discussed by Ayachi *et al.* for Ag and n-type $Mg_2(Si,Sn)$ [37]. However, it is unlikely that the mechanism at play in our case is similar. For Ag, a *local gradient* in the Seebeck coefficient was observed from the interfaces to the center of the TE material. If Al was a faster or a similar diffuser in $Mg_2(Si,Sn)$ compared to Ag, a change in the Seebeck coefficient would be observed directly after joining, which is not the case. If Al was a slower diffuser the formation of a gradient would be expected upon annealing time, which is in contrast to the observed constant change along the TE material.

Moreover, Ag is well-known as a p-type dopant for $Mg_2(Si,Sn)$, it is therefore plausible that its diffusion into the n-type material decreases its carrier concentration. On the other hand Al was predicted and shown to be a rather poor dopant in $Mg_2(Si,Sn)$ [62-66], with the data focusing on the Si-rich side of the spectrum. In our case of hypothetical uncontrolled Al-doping, the effect on carrier concentration would therefore be expected to be rather weak. DFT calculations similar to those made for Ag [37] should be considered for Al in order to

understand which defects it creates in the TE material and how this could affect the carrier concentration on the Sn-rich end of the composition range.

Finally, the mobility calculations in Table 2 show that the mobility is decreasing at the same time as the carrier concentration, resulting in a larger decrease of the electrical conductivity. The loss of mobility is similar for all samples. It has already been shown that one consequence of Mg loss is the decrease in charge carriers mobility [49, 56], while from a simple carrier concentration reduction (by counter-doping) no loss in mobility would be expected.

All this suggests that the observed changes in the material properties are due to Mg loss rather than Al diffusion leading to a charge carrier compensation. We also note that the difference in S variation could also be indicating a lack of reproducibility in the BN-coating quality and thus extend of Mg evaporation. For a further confirmation of the drawn conclusions further investigations and annealing experiments should be performed with better coating, see e.g. [67-72].

A summary of the results obtained for aluminum and the electrodes previously reported in literature can be found in Table 3. It shows that aluminum is the best electrode so far for contacting p-type and n-type $Mg_2(Si,Sn)$ with optimal TE properties.

Table 3 - Summary of the contact resistance and limitations of potential electrodes for $Mg_2Si_{1-x}Sn_x$ with $x=0.3 - 0.4$

Electrode	r_c ($\mu\Omega\text{cm}^2$)	Evaluation after joining	Evaluation after annealing	Reference
Ni	25-50	Cracks due to CTE mismatch	No annealing experiment	[32]
Ag	9-15	Electrode-induced decrease in n-type carrier concentration	No annealing experiment	[32, 37]
Cu	<10	Electrode-induced decrease in n-type carrier concentration; thick reaction layer which can cause delamination	Further decrease in n-type carrier concentration, probably both due to electrode and Mg loss	[38]
CuNi	<50	Electrode-induced decrease in n-type carrier concentration; cracks due to CTE mismatch	No annealing experiment	[38]
Al	≤ 10	Fine	Decrease in n-type carrier concentration,	This work

			presumably due to Mg loss	
--	--	--	---------------------------	--

Conclusion

We found a suitable material and joining conditions to make stable and high quality contact for a Mg₂(Si,Sn) material system. Obtained joints are mechanically and chemically stable after 2 weeks of annealing. Contacting at 500°C leads to low electrical contact resistances, around 10 $\mu\Omega\text{cm}^2$ for both n- and p-type materials and no deterioration of those values is observed after annealing. The p-type properties are found to be stable, while a variable change in the n-type Seebeck coefficient is observed after annealing. It is attributed to magnesium evaporation from the TE material and presumably not due to the interaction between the electrode and the TE material, unlike previous electrodes like Ag and Cu which showed counter-doping effects [33, 37]. Although it is still suggested to add a protection layer on the TE material for enhanced material stability and preserved maximum efficiency, aluminum is shown to be a very promising electrode for a future Mg₂(Si,Sn)-based thermoelectric generator.

Conflicts of interest

The authors declare no competing financial interest.

Acknowledgements

The authors would like to gratefully acknowledge the endorsement for the DLR executive Board Members for Space Research and Technology, as well as the financial support from the Young Research Group Leader Program. M.Y. would like to thank for his financial support which is provided by the DFG via the GRK (Research Training Group) 2204 "Substitute Materials for Sustainable Energy Technologies". G.C.H would like to thank the financial support of the Mexican Science and Technology Ministry (CONACyT). J.C., N.H.P, D.Y.N.T., N.F and would like to thank the DAAD fellowship programs (No. 57424731, 57265854, 57370121 and 248, respectively), while JdB is partially funded by the Deutsche Forschungsgemeinschaft (DFG, German Research Foundation), project number 396709363. Lastly, we would also like to acknowledge Paweł Ziolkowski and Przemysław Blaschkewitz for their help and assistance with the thermoelectric measurements as well as S. Ayachi for discussions.

Data Availability Statement:

The raw/processed data required to reproduce these findings cannot be shared at this time due to legal or ethical reasons.

References

1. Karella, S., et al., *Energetic and exergetic analysis of waste heat recovery systems in the cement industry*. Energy, 2013. **58**: p. 147-156.
2. Yang, J. and F. Stabler, *Automotive Applications of Thermoelectric Materials*. Journal of Electronic Materials, 2009. **38**: p. 1245–1251 (2).
3. Snyder, G.J. and E.S. Toberer, *Complex thermoelectric materials*, in *Materials for sustainable energy: a collection of peer-reviewed research and review articles from Nature Publishing Group*. 2011, World Scientific. p. 101-110.
4. He, R., G. Schierning, and K. Nielsch, *Thermoelectric Devices: A Review of Devices, Architectures, and Contact Optimization*. Advanced Materials Technologies, 2018. **3**(4): p. 1700256.
5. Rowe, D. and G. Min, *Design theory of thermoelectric modules for electrical power generation*. IEE Proceedings-Science, Measurement, 1996. **143**(6): p. 351-356.
6. Rowe, D., *Conversion efficiency and figure-of-merit*, in *CRC Handbook of thermoelectrics*. 1995, CRC press. p. 31-37.
7. de Boor, J., et al., *Recent progress in p-type thermoelectric magnesium silicide based solid solutions*. Materials Today Energy, 2017. **4**: p. 105-121.
8. Bashir, M.B.A., et al., *Recent advances on Mg₂Si_{1-x}Sn_x materials for thermoelectric generation*. Renewable Sustainable Energy Reviews, 2014. **37**: p. 569-584.
9. de Boor, J., et al., *Thermoelectric performance of Li doped, p-type Mg₂ (Ge, Sn) and comparison with Mg₂ (Si, Sn)*. Acta Materialia, 2016. **120**: p. 273-280.
10. Zaitsev, V., et al., *Highly effective Mg₂Si_{1-x}Sn_x thermoelectrics*. Physical Review B, 2006. **74**(4): p. 045207.
11. Fedorov, M.I., V.K. Zaitsev, and G.N. Isachenko. *High effective thermoelectrics based on the Mg₂Si-Mg₂Sn solid solution*. in *Solid State Phenomena*. 2011. Trans Tech Publ.
12. Liu, W., et al., *Convergence of conduction bands as a means of enhancing thermoelectric performance of n-type Mg₂Si_{1-x}Sn_x solid solutions*. Physical Review Letters, 2012. **108**(16): p. 166601.
13. Trivedi, V., et al., *Microstructure and doping effect on the enhancement of the thermoelectric properties of Ni doped Dy filled CoSb₃ skutterudites*. Sustainable Energy Fuels, 2018. **2**(12): p. 2687-2697.
14. Muthiah, S., et al., *Significant enhancement in thermoelectric performance of nanostructured higher manganese silicides synthesized employing a melt spinning technique*. Nanoscale, 2018. **10**(4): p. 1970-1977.
15. Ostovari Moghaddam, A., et al., *Ge-Doped ZnSb/β-Zn₄Sb₃ Nanocomposites with High Thermoelectric Performance*. Advanced Materials Interfaces, 2019. **6**(18): p. 1900467.
16. Jood, P., et al., *Na Doping in PbTe: Solubility, Band Convergence, Phase Boundary Mapping, and Thermoelectric Properties*. Journal of the American Chemical Society, 2020. **142**(36): p. 15464-15475.
17. Song, K.-M., et al., *Synthesis and Thermoelectric Properties of Ce 1-z Pr z Fe 4-x Co x Sb 12 Skutterudites*. Journal of Electronic Materials, 2017. **46**(5): p. 2634-2639.
18. Yang, S., et al., *Thermal stability study of melt spun TAGS-80 thermoelectric bulks*. Journal of Materials Science: Materials in Electronics, 2017. **28**(20): p. 15279-15283.

19. Tani, J.-i. and H. Kido, *Fabrication and thermoelectric properties of Mg₂Si-based composites using reduction reaction with additives*. *Intermetallics*, 2013. **32**: p. 72-80.
20. Skomedal, G., et al., *Design, assembly and characterization of silicide-based thermoelectric modules*. *Energy Conversion and Management*, 2016. **110**: p. 13-21.
21. de Padoue Shyikira, A., G. Skomedal, and P.H. Middleton, *Performance evaluation and stability of silicide-based thermoelectric modules*. *Materials Today: Proceedings*, 2020.
22. Kaibe, H., et al. *Development of thermoelectric generating stacked modules aiming for 15% of conversion efficiency*. in *ICT 2005. 24th International Conference on Thermoelectrics, 2005*. 2005. IEEE.
23. Tarantik, K.R., et al., *Thermoelectric Modules Based on Silicides—Development and Characterization*. *Materials Today: Proceedings*, 2015. **2**(2): p. 588-595.
24. Nakamura, T., et al., *Power-Generation Performance of a π-Structured Thermoelectric Module Containing Mg₂Si and MnSi 1.73*. *Journal of Electronic Materials*, 2015. **44**(10): p. 3592-3597.
25. Kim, H.S., et al., *Design of segmented thermoelectric generator based on cost-effective and light-weight thermoelectric alloys*. *Materials Science Engineering: B*, 2014. **185**: p. 45-52.
26. Tohei, T., et al. *Bondability of Mg₂Si element to Ni electrode using Al for thermoelectric modules*. in *IOP Conference Series. Materials Science and Engineering (Online)*. 2014.
27. Gao, P., *Mg₂(Si, Sn)-based thermoelectric materials and devices*. 2016, Michigan State University: Michigan State University. p. 128.
28. Skomedal, G., et al., *High temperature oxidation of Mg₂(Si-Sn)*. *Corrosion Science*, 2016. **111**: p. 325-333.
29. Shirzadi, A., H. Assadi, and E. Wallach, *Interface evolution and bond strength when diffusion bonding materials with stable oxide films*. *Surface and Interface Analysis*, 2001. **31**(7): p. 609-618.
30. Li, S.-L., et al. *Thermo-mechanical analysis of thermoelectric modules*. in *2010 5th International Microsystems Packaging Assembly and Circuits Technology Conference*. 2010. IEEE.
31. D'Angelo, J.J., et al., *Electrical Contact Fabrication and Measurements of Metals and Alloys to Thermoelectric Materials*. *Materials Research Society Symposium Proceedings*, 2008. **1044**: p. 449-455.
32. Pham, N.H., et al., *Ni and Ag electrodes for magnesium silicide based thermoelectric generators*. *Materials Today Energy*, 2019. **11**: p. 97-105.
33. Ayachi, S., et al., *Developing Contacting Solutions for Mg₂Si_{1-x}Sn_x-Based Thermoelectric Generators: Cu and Ni₄₅Cu₅₅ as Potential Contacting Electrodes*. *ACS Applied Materials Interfaces*, 2019. **11**(43): p. 40769-40780.
34. de Boor, J., et al., *Fabrication and characterization of nickel contacts for magnesium silicide based thermoelectric generators*. *Journal of Alloys and Compounds*, 2015. **632**: p. 348-353.
35. de Boor, J., et al., *Thermal stability of magnesium silicide/nickel contacts*. *Journal of Electronic Materials*, 2016. **45**(10): p. 5313-5320.
36. Mitra, K., S. Mahapatra, and T. Dasgupta, *Fabrication of Nickel Contacts for Mg₂Si Based Thermoelectric Generators via an Induction Assisted Rapid Monoblock Sintering Technique*. *Journal of Electronic Materials*, 2019. **48**(3): p. 1754-1757.
37. Ayachi, S., et al., *On the Relevance of Point Defects for the Selection of Contacting Electrodes: Ag as an Example for Mg₂(Si,Sn)-based Thermoelectric Generators*. *Materials Today Physics*, 2021. **16**: p. 100309.
38. Ayachi, S., et al., *Contacting Cu Electrodes to Mg₂Si 0.3 Sn 0.7: Direct vs. Indirect Resistive Heating*. *Semiconductors*, 2019. **53**(13): p. 1825-1830.
39. Zwolenski, P., J. Tobola, and S. Kaprzyk, *A theoretical search for efficient dopants in Mg₂X (X=Si, Ge, Sn) thermoelectric materials*. *Journal of Electronic Materials*, 2011. **40**(5): p. 889-897.
40. Tani, J.-i. and H. Kido, *First-principles and experimental studies of impurity doping into Mg₂Si*. *Intermetallics*, 2008. **16**(3): p. 418-423.

41. Nix, F. and D. MacNair, *The thermal expansion of pure metals: copper, gold, aluminum, nickel, and iron*. Physical Review, 1941. **60**(8): p. 597.
42. Gelbstein, Y., et al., *Physical, mechanical, and structural properties of highly efficient nanostructured n-and p-silicides for practical thermoelectric applications*. Journal of Electronic Materials, 2014. **43**(6): p. 1703-1711.
43. Murray, J. and A. McAlister, *The Al-Si (aluminum-silicon) system*. Bulletin of Alloy Phase Diagrams, 1984. **5**(1): p. 74.
44. McAlister, A. and D. Kahan, *The Al- Sn (aluminum-tin) system*. Bulletin of Alloy Phase Diagrams, 1983. **4**(4): p. 410-414.
45. Li, Z., et al., *Control of Mg₂Sn formation through ultrasonic-assisted transient liquid phase bonding of Mg to Al*. Journal of Materials Processing Technology, 2018. **255**: p. 524-529.
46. Bartur, M. and M.-A. Nicolet, *Aluminum contact to nickel silicide using a thin tungsten barrier*. Thin Solid Films, 1982. **91**(2): p. 89-98.
47. Kajikawa, T., et al. *Thermoelectric properties and electrode bonding performance for metal silicides*. in *Proceedings ICT2001. 20 International Conference on Thermoelectrics (Cat. No. 01TH8589)*. 2001. IEEE.
48. Farahi, N., et al., *High efficiency Mg₂ (Si, Sn)-based thermoelectric materials: scale-up synthesis, functional homogeneity, and thermal stability*. RSC Advances, 2019. **9**(40): p. 23021-23028.
49. Sankhla, A., et al., *Analyzing thermoelectric transport in n-type Mg₂SiO₄SnO₆ and correlation with microstructural effects: An insight on the role of Mg*. Acta Materialia, 2020.
50. Kamila, H., et al., *Synthesis of p-type Mg₂Si_{1-x}Sn_x with x=0-1 and optimization of the synthesis parameters*. Materials Today: Proceedings, 2019. **8**: p. 546-555.
51. Platzek, D., et al. *Potential-Seebeck-microprobe (PSM): measuring the spatial resolution of the Seebeck coefficient and the electric potential*. in *ICT 2005. 24th International Conference on Thermoelectrics, 2005*. 2005. IEEE.
52. Kamila, H., et al., *Analyzing transport properties of p-type Mg₂Si-Mg₂Sn solid solutions: optimization of thermoelectric performance and insight into the electronic band structure*. Journal of Materials Chemistry A, 2019. **7**(3): p. 1045-1054.
53. Farahi, N., et al., *Nano-and microstructure engineering: an effective method for creating high efficiency magnesium silicide based thermoelectrics*. ACS Applied Materials Interfaces, 2016. **8**(50): p. 34431-34437.
54. Schroder, D.K., *Semiconductor material and device characterization*. 2015: John Wiley & Sons.
55. Ziolkowski, P., et al., *Probing thermopower on the microscale*. physica status solidi, 2013. **210**(1): p. 89-105.
56. Kato, D., et al., *Control of Mg content and carrier concentration via post annealing under different Mg partial pressures for Sb-doped Mg₂Si thermoelectric material*. Journal of Solid State Chemistry, 2018. **258**: p. 93-98.
57. Kasai, H., et al., *Multi-temperature structure of thermoelectric Mg₂Si and Mg₂Sn*. Acta Crystallographica Section B: Structural Science, Crystal Engineering Materials, 2017. **73**(6): p. 1158-1163.
58. Rittiruam, M., et al., *Predication of Thermal Conductivity of Mg₂X (X= Ge and Sn) by Molecular Dynamics*. Integrated Ferroelectrics, 2015. **165**(1): p. 61-72.
59. Evans, A. and E. Charles, *Strength recovery by diffusive crack healing*. Acta Metallurgica, 1977. **25**(8): p. 919-927.
60. Chou, I.A., H.M. Chan, and M.P. Harmer, *Effect of annealing environment on the crack healing and mechanical behavior of silicon carbide-reinforced alumina nanocomposites*. Journal of the American Ceramic Society, 1998. **81**(5): p. 1203-1208.
61. Liu, X., et al., *Significant roles of intrinsic point defects in Mg₂X (X= Si, Ge, Sn) thermoelectric materials*. Advanced Electronic Materials, 2016. **2**(2): p. 1500284.

62. Vivekanandhan, P., et al., *Structural features and thermoelectric properties of spark plasma assisted combustion synthesised Magnesium silicide doped with Aluminium*. Materials Chemistry and Physics, 2020. **241**: p. 122407.
63. Tani, J.-i. and H. Kido, *Thermoelectric properties of Al-doped Mg₂Si_{1-x}Sn_x ($x \leq 0.1$)*. Journal of Alloys and Compounds, 2008. **466**(1-2): p. 335-340.
64. Hu, X., M.R. Barnett, and A. Yamamoto, *Synthesis of Al-doped Mg₂Si_{1-x}Sn_x compound using magnesium alloy for thermoelectric application*. Journal of Alloys and Compounds, 2015. **649**: p. 1060-1065.
65. Kim, G., et al., *Co-doping of Al and Bi to control the transport properties for improving thermoelectric performance of Mg₂Si*. Scripta Materialia, 2016. **116**: p. 11-15.
66. Kato, A., T. Yagi, and N. Fukusako, *First-principles studies of intrinsic point defects in magnesium silicide*. Journal of Physics: Condensed Matter, 2009. **21**(20): p. 205801.
67. Battiston, S., et al., *Multilayered thin films for oxidation protection of Mg₂Si thermoelectric material at middle-high temperatures*. Thin Solid Films, 2012. **526**: p. 150-154.
68. D'Isanto, F., et al., *Oxidation protective glass coating for magnesium silicide based thermoelectrics*. Ceramics International, 2020. **46**(15): p. 24312-24317.
69. Gucci, F., et al., *Oxidation protective hybrid coating for thermoelectric materials*. Materials, 2019. **12**(4): p. 573.
70. Nieroda, P., et al., *New high temperature amorphous protective coatings for Mg₂Si thermoelectric material*. Ceramics International, 2019. **45**(8): p. 10230-10235.
71. Sadia, Y., D. Ben-Ayoun, and Y. Gelbstein, *PbO-SiO₂-based glass doped with B₂O₃ and Na₂O for coating of thermoelectric materials*. Journal of Materials Research, 2019. **34**(20): p. 3563-3572.
72. Tani, J.-i., M. Takahashi, and H. Kido, *Fabrication of oxidation-resistant β -FeSi₂ film on Mg₂Si by RF magnetron-sputtering deposition*. Journal of Alloys and Compounds, 2009. **488**(1): p. 346-349.